

Effectiveness of the dispersed-phase continuum model for investigating the airflow in the print gap of inkjet printers

A. F. V. de A. Aquino ^{1,2,*}, S. G. Mallinson ^{1,2}, G. D. McBain ², G. D. Horrocks ²,
C. M. de Silva,¹ and T. J. Barber¹

¹*School of Mechanical & Manufacturing Engineering, University of New South Wales, Sydney, New South Wales 2052, Australia*

²*Memjet, Macquarie Park, New South Wales 2113, Australia*



(Received 5 July 2022; accepted 28 June 2023; published 7 September 2023)

To investigate the effectiveness of the dispersed-phase continuum (DPC) approximation to model the airflow in the print gap of inkjet printers, three-dimensional simulations using the DPC model were compared against those using the classic particle-in-cell (P-in-C) approach. The DPC approximation, due to the separation of time scales, models the dispersed phase with a momentum source that depends on a predefined temporally averaged particle number density field. The results demonstrated that the steady DPC model correlated well to the time-averaged P-in-C solution when the former's formulation accounted for the droplet deceleration. The steady DPC model requires less than 0.1% of the computational resources used by the transient P-in-C approach to compute the mean flow field. Further analyses indicated that the DPC model captured a supercritical pitchfork bifurcation, where the airflow shifted from a steady spanwise uniform regime to a standing wave regime at a critical number density. The P-in-C model computed a smooth continuous transition that characterizes an excited supercritical pitchfork bifurcation. An excellent correlation between the models was observed at print densities above the transition point, but at low number densities a certain level of discrepancy was observed. This was a result of the *pseudoturbulence* or *spottiness* induced by the local and instantaneous motion of droplets that excited the standing wave solution even at low number densities. The results, thus, demonstrated that the DPC model is effective at estimating the mean flow field and approximating the bifurcation diagram, while being simultaneously more computationally efficient than the P-in-C model.

DOI: [10.1103/PhysRevFluids.8.094302](https://doi.org/10.1103/PhysRevFluids.8.094302)

I. INTRODUCTION

The inkjet printing industry faces the challenge of developing systems that can operate at large print gap heights ($H > 1$ mm) [1–3] to enable the expansion of inkjet technology to applications, such as rapid prototyping, manufacturing of electronics, solar panels, and reinforced composites. Restrictive print gap heights in current designs prevent inkjet systems from accommodating media with variable or large thickness and increase the likelihood of the media striking the printhead and damaging the nozzles. Further, at high print heights, aerodynamic effects tend to misplace the ink droplets on the paper, creating printing defects such as tiger stripes and/or wood grain [4–10].

These printing defects have been found to be associated with the airflow nonuniformity in time and span direction across the print zone [5–7,11]. The relative motion between the ink droplets and the surrounding air creates two counter-rotating vortices and, at specific operating conditions, these

*andre.aquino@unsw.edu.au

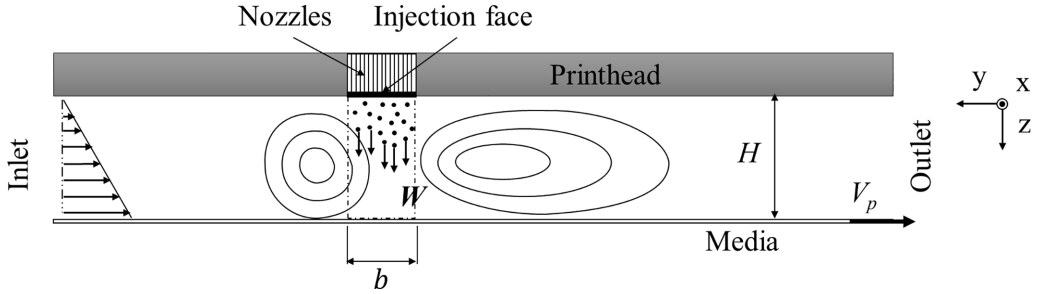


FIG. 1. Schematic of the physics in the numerical model where the origin of the system is located at the center of the injection face.

become unstable [4,8,9]. Mallinson *et al.* [12] demonstrated, using numerical analyses based on the dispersed-phase continuum (DPC) model, the existence of three different airflow regimes. At large b/H , where b is the breadth of the print zone (Fig. 1), the airflow is stable and uniform in time and span direction (x direction), while at smaller b/H the airflow is unsteady. At intermediate b/H , however, the airflow is uniform in time but nonuniform in the span direction as it shows a spanwise periodicity. In this regime, the airflow's x velocity varies in a sinusoidal pattern and the main vortex becomes deformed with a standing wave pattern evident.

The airflow nonuniformity can then misplace the droplets on the paper, inducing the print pattern characteristic of tiger stripes. We note here that one of the mechanisms that creates regions with higher optical density on the paper is a result of the misplacement of satellite droplets. The satellite droplets have lower Stokes number, $S < 1$, with

$$S = \frac{\rho_d d^2 W}{18\mu H}, \quad (1)$$

where ρ_d is the droplet density, d is the diameter of the droplet, μ is the dynamic viscosity of air, and W is the droplet ejection velocity [7]. This means that the satellite droplets are more likely to be carried by the airflow instability, landing away from the main drops and covering the white spaces between lines as seen in Fig. 2, which has been reproduced from Mallinson *et al.* [12]. From Fig. 2, it is also observed on the left and right sides of the bottom image that, depending on the operating conditions, the main droplets can be minimally affected by the airflow. This is supported by the fact that the linewidth and space between lines are consistent across the width of the page. Another mechanism that is expected to induce the variation in optical density is related to the divergence of the misplacement of both main and satellite droplets [7,12]. The main drop and satellite divergence fields have their respective influence coefficients that depend on dot size, print density, and misplacement magnitude that impact on the optical density variation. Since, in this study, focus is given to investigate the conditions at the onset of spanwise nonuniformity, it is expected that the main droplets are not sufficiently deflected to change their effect on the airflow.

Print samples provided by Memjet [13] have indicated the existence of similar regimes as observed in the simulations. At low duty cycles (fraction of nozzles activated during printing) and b/H ratios, the prints tend to be uniform (flat gray), but with higher duty cycles and/or aspect ratios the prints develop a spanwise periodicity characterized by vertical bands with different optical density. With further increments in duty cycles and/or aspect ratios, the prints appear more nonuniform in the longitudinal direction. It is believed that these printing patterns relate to the flow regimes identified in Mallinson *et al.* [12]. While the temporally nonuniform (unsteady) airflow leads to longitudinally nonuniform prints, the spanwise flow field variation of the standing waves creates the reported vertical stripes. The different flow regimes and their respective impact on prints of uniform image density are summarized in Fig. 3. This manuscript focuses on investigating the transition from the aforementioned uniform regime to the standing wave regime as this transition is expected to define the bounds of the printing envelope at which the prints are uniform.

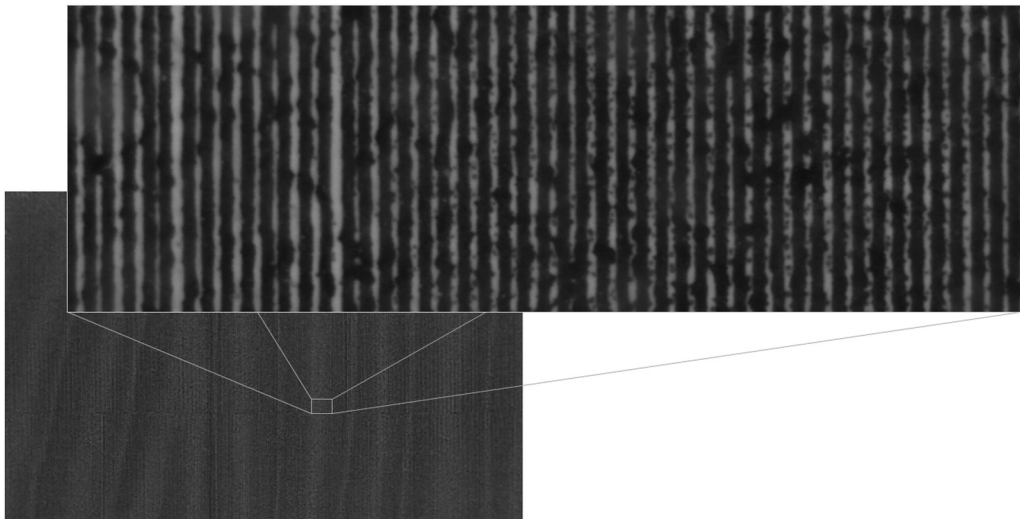


FIG. 2. Example print of a 10% green noise gray image where the nonuniform air flow in the print zone gives rise to optical density variations. The magnified region shows the optical density variations are caused by misplaced satellites which are much smaller than the main droplets. Image reproduced from Mallinson *et al.* [12].

The numerical analyses conducted by de A. Aquino *et al.* [4], Mallinson *et al.* [12], de A. Aquino *et al.* [14] introduced the DPC model to investigate the entrainment effect of the dispersed phase (ink droplets). This model was introduced as a less computationally expensive alternative to the classic particle-in-cell (P-in-C) or Lagrangian model that had already been implemented to investigate the entrainment effect [7,11,15]. The P-in-C and the DPC approaches, along with the direct numerical simulations [16,17] and Eulerian-Eulerian models [18,19], are part of a wide variety of models that deal with the same challenge of being computationally efficient, while accurately predicting the dynamics of particle-driven flows [18].

The P-in-C model employs dynamic equations to track each individual particle of the dispersed phase while treating the fluid phase as a continuum [18–21]. The DPC approximation models the dispersed phase with a momentum source that depends on a predefined temporally averaged particle number density field [4,12,14]. This assumption eliminates the need of solving the dynamic equations to calculate the number density in each specific cell as seen in the P-in-C model and is expected to reduce the computational cost of the simulations. While a preliminary comparison of the flow features predicted by the DPC and P-in-C models and those evident in experimental, time-averaged, laser light-sheet visualization has already been presented [12], further investigation needs to be undertaken to assess the effectiveness of the DPC model. In this manuscript, the effectiveness of the DPC model for predicting the change from a uniform regime to a standing wave regime is investigated and compared against the results using the P-in-C model.

II. METHODOLOGY

A. Numerical model

Both P-in-C and DPC models solve the continuity and momentum equations for incompressible laminar flows and assume the droplets as point sources:

$$\frac{\partial \mathbf{u}}{\partial t} + \mathbf{u} \cdot \nabla \mathbf{u} = -\frac{1}{\rho} \nabla p + \mathbf{F} + \nu \nabla^2 \mathbf{u}, \quad (2)$$

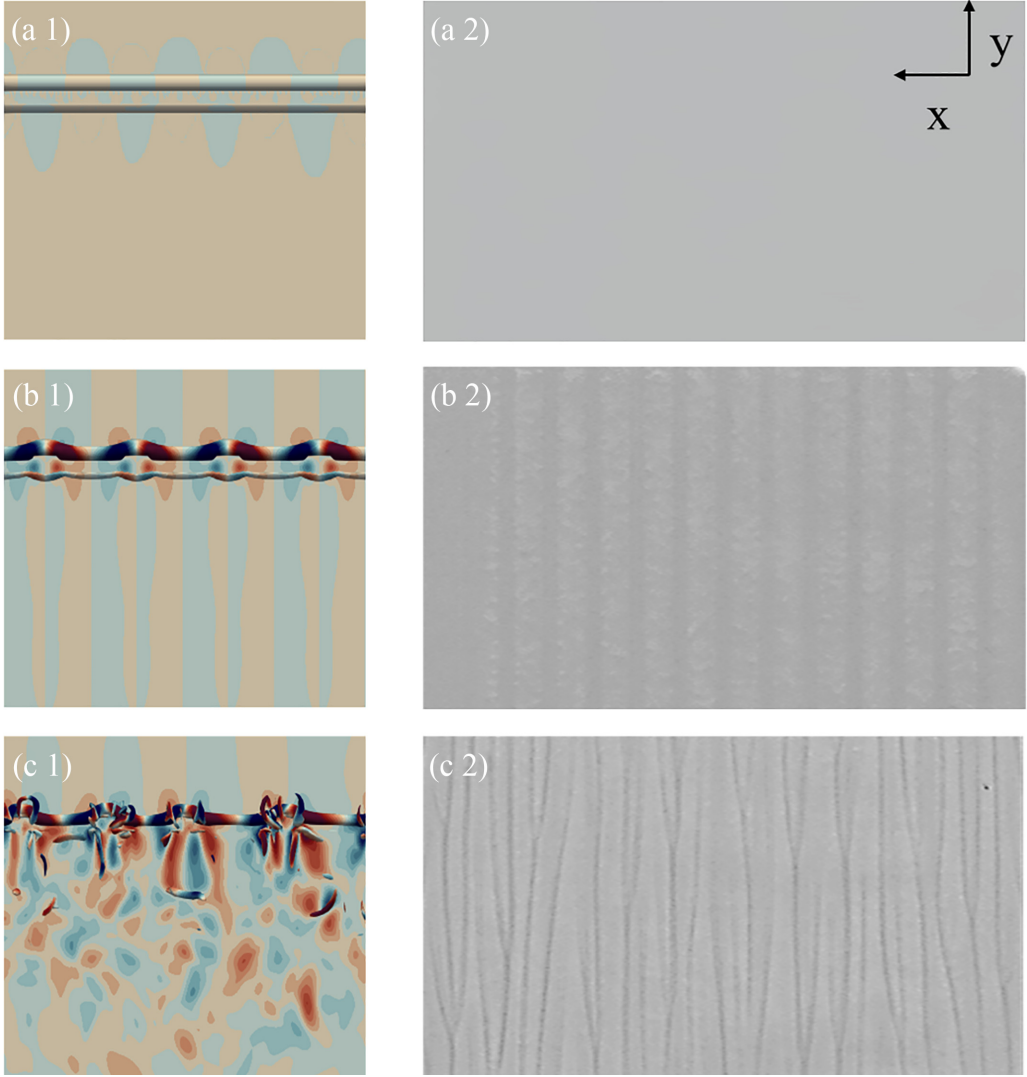


FIG. 3. On the left: flow field snapshots adapted from Mallinson *et al.* [12]; on the right side: prints of flat gray on an A4 page provided by Memjet with print speed of 0.41 m/s and green noise of 10%; (a2) $b/H = 1/2.2$, (b2) $b/H = 1/3.2$, and (c2) $b/H = 1/4$.

$$\nabla \cdot \mathbf{u} = 0, \quad (3)$$

where \mathbf{u} is the velocity field, t is time, p is pressure, ν is the air kinematic viscosity, and \mathbf{F} is the force per unit mass induced by the dispersed phase moving at velocity \mathbf{u}_d , where the subscript d refers to the dispersed or particle phase.

The P-in-C model, implemented in the OpenFOAM solver reactingParcelFoam, computes the body force in the k -th cell (\mathbf{F}_k) and at a given time step as the summation of the forces exerted by q number of particles located in that k -th cell, where \mathbf{f}_k^m represents the force exerted by the m -th particle. We note here that, due to the separation between droplets and cell sizes tested in this study, q is either 0 or 1 and Eq. (4) reduces to Eq. (5). The P-in-C model demands yet additional equations to track the motion of droplets over time. The position of the m -th particle with volume v_d

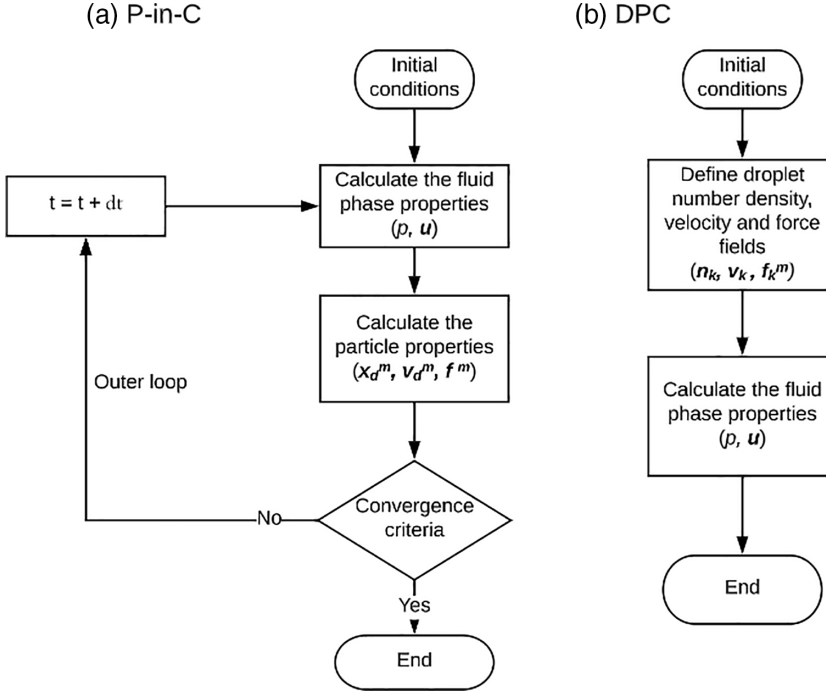


FIG. 4. Flow chart exhibiting the solution algorithm for the P-in-C (a) and DPC (b) models.

is given by the kinematic equation of motion [Eq. (6)] and Newton's second law is used to compute the particle velocity [Eq. (7)]. Figure 4(a) shows the process used by the P-in-C model to compute the solution:

$$\mathbf{F}_k = \sum_{m=1}^{m=q} \mathbf{f}_k^m, \quad (4)$$

$$\mathbf{F}_k = \begin{cases} f_k^1 & \text{if } q = 1, \\ 0 & \text{otherwise,} \end{cases} \quad (5)$$

$$\frac{d\mathbf{x}_d^m}{dt} = \mathbf{u}_d^m, \quad (6)$$

$$v_d \rho_d \frac{d\mathbf{u}_d^m}{dt} = \mathbf{f}^m. \quad (7)$$

In the dispersed-phase continuum (DPC) model, the dispersed properties are defined beforehand [Fig. 4(b)]. Due to the separation of time scales (droplet relaxation time, flow characteristic time, droplet transit time, and time difference between droplets visiting the k -th cell), it is assumed that the force term on the k -th cell with volume v_k is governed by the expected temporally averaged rate of visitation of the particles at the respective cell (n_k):

$$\mathbf{F}_k = v_k n_k \mathbf{f}_k^m. \quad (8)$$

In both models, \mathbf{f}^m is equal, but of opposite sign, to the drag the droplets experience and is modeled with the Stoke's law multiplied by an empirical correction factor [Eq. (9)] $1 + \varphi$ determined by White [22] [Eq. (10)]. This method is based on a fit to experimental data for Reynolds number less than 200 000, which covers the range of droplet Reynolds number (Re_d) tested in this

study, which is approximately $4.5 < \text{Re}_d < 16$ ($\text{Re}_d = \frac{|\mathbf{u}_d - \mathbf{u}|d}{\nu}$). The Reynolds number for the flow across the print gap, on the other hand, is given by $\text{Re}_H = \frac{V_p H}{\nu}$ and is equal to 81:

$$\mathbf{f}^m = 3\pi\mu(\mathbf{u}_d^m - \mathbf{u})[1 + \varphi(\text{Re}^m)], \quad (9)$$

$$\varphi(\text{Re}_d) = \frac{\text{Re}_d}{4(1 + \sqrt{\text{Re}_d})} + \frac{\text{Re}_d}{60}. \quad (10)$$

To couple the pressure and momentum equations in both models, the *PIMPLE* scheme [23] is employed here due to its robustness. It is deemed that the outer loop of the *PIMPLE* scheme has reached convergence when the pressure and momentum residuals fall to less than 10^{-5} , as suggested by Holzmann [23]. Pure Crank–Nicolson, a second-order implicit scheme, is used to discretize the time derivative, while the second-order discretization of the gradient, divergence, and Laplacian terms is achieved via the unbounded central-differencing algorithm, named Gauss linear in the OpenFOAM idiom [23]. The velocity terms are solved using the biconjugate gradient method with a diagonal incomplete LU preconditioner [24], while the geometric algebraic multigrid method is used to solve the pressure equation, with diagonal incomplete Cholesky Gauss-Seidel smoothing [25].

B. Geometry and boundary condition

A rectangular cuboid domain was created to reproduce the print gap defined by the printhead and the media (see Fig. 1). The media is a wall moving at V_p in the negative y direction and located at $z = 0$, while the printhead surface is modeled as a stationary wall and is located at $z = -H$. The lateral boundaries are located w apart to compute the wavelength with sufficient resolution and are set as periodic boundaries. The injection zone, i.e., the region where the droplets are fired from the injection face, has length $b = 1/3H$ extending throughout the span of the domain. For the DPC model, w is equal to $15H$ but, for the P-in-C model, due to the excessive computational cost of the simulations, $w = 1.875H$ or $1/8$ of $15H$, which is equal to the wavelength of one possible solution observed in the DPC simulations. This allows the P-in-C model to time resolve the standing wave without significantly affecting the flow field spatial resolution.

The inlet and outlet are respectively located $8.33H$ upstream and $15H$ downstream of the print zone to allow the flow to fully develop. While the outlet has a specified constant pressure, the inlet is set with a Couette–Poiseuille velocity profile. The Couette component is induced by the paper motion, while the Poiseuille component is a result of the pressure gradient created by aerosol suction systems and the drag created by the droplets. The velocity profile is, then, derived from the through-flow parameter, χ , which is the ratio of the added (Poiseuille) flow rate, q_a , to the paper-induced (Couette) flow rate, q_p , where \bar{V}_a is the average velocity of the Poiseuille part:

$$\chi = \frac{q_a}{q_p} = 2\frac{\bar{V}_a}{V_p}. \quad (11)$$

In this study, the temporally averaged number density (n) used in the DPC model is defined by Eq. (12), where it depends on the number of firing locations (active nozzles) per unit area on the injection face (σ), the firing frequency (f), and \mathbf{u}_d . The number of active nozzles per unit area is given by $\sigma = r\xi/\Delta x b$, where ξ is the duty cycle which represents the fraction of nozzles that are activated with $0 \leq \xi \leq 1$ and b and w are the injection-zone breadth and width (out of the page in Fig. 1), respectively. To begin with, the droplet velocity was set as constant, disregarding the droplet deceleration. The impact of this assumption on the accuracy of the model is further described in the Results section:

$$n = \frac{\sigma f}{|\mathbf{u}_d|}. \quad (12)$$

C. Governing dimensionless parameters

Equation (2) is nondimensionalized using the ejection droplet speed W and the print gap height H as the characteristic scales. Given that the problem is defined by eight parameters— W , d , H , b , V_p , n , ν , and \bar{V}_a —that have two dimensions, there must be six groups of dimensionless parameters governing this system, which are N , R , b/H , Re_d , V_p/W , and χ . N is the dimensionless number density of drops given by $N = n_o d H \nu / W$, where n_o is n at the injection face and R represents the transit Reynolds number ($R = HW/\nu = 2978$). The additional governing dimensionless parameters are the dimensionless print gap height or aspect ratio ($b/H = 1/3$), droplet Reynolds number ($Re_d = Wd/\nu = 15.5$), dimensionless paper speed ($V_p/W = 0.027$), and dimensionless through-flow ($\chi = 0$). Here, the continuum phase (air) has kinematic viscosity of $\nu = 0.015 \text{ mm}^2 \text{ ms}^{-1}$. The droplets are ejected with velocity of $W = 14.95 \text{ m/s}$ at a firing rate of $f = 15.5 \text{ kHz}$ and are assumed to be solid spheres with diameter of $d = 15.6 \text{ }\mu\text{m}$ [12].

D. Flow metrics

The spanwise component of the airflow velocity (u_x) is the main metric used to correlate the misplacement of droplets on the paper to the flow features observed in the simulations. This is because the optical density variation seen in Fig. 3(b2) primarily occurs in the spanwise direction, indicating that it is linked to variations in u_x . To measure this variation in the flow field, a spanwise transect and a plane, both located at $z/H = -0.5$, were used in our analyses. The root mean square (rms) of the u_x profile along the spanwise transect is then further calculated to quantify the strength of the standing wave.

To aid in the investigation of changes in the structure of the main vortex, isosurfaces and contours of Q criterion are employed. The Q criterion has been used in different applications to efficiently identify vortices. This relates to its formulation that subtracts the strain rate part of the vorticity magnitude [Eq. (13)]. When $Q > 0$, the vorticity exceeds the strain rate, indicating the existence of a vortex. We note that the dimensionless Q criterion is given by $\tilde{Q} = Q(H/W)^2$, while the dimensionless velocity is $\tilde{u} = u/W$:

$$Q = \frac{1}{2} (|\Omega|^2 - |S|^2). \quad (13)$$

E. Transient statistics

Unsteady flows, as measured in the P-in-C simulations, tend to present an initial transient phase (startup) where the flow develops from the initial conditions. To eliminate this startup effect and determine the interval that the signal is statistically stationary, the transient scanning technique (TST) is employed. The TST calculates the uncertainty of the mean for a 95% confidence level and determines the interval at which the uncertainty of the mean exponentially decays with the realization time, characterizing a stationary signal [26].

The TST applied to the rms of the lateral airflow velocity measured by a transect indicates that the startup effect can take up to 200 000 time steps. The uncertainty of the mean for the stationary regime tends to be lower than 0.2%. This low uncertainty level is likely to be due to the long realization times that reach up to 400 000 time steps. For the remainder of this manuscript, the mean values of the P-in-C simulations refer only to the stationary interval of the signal.

F. Spatial discretization

The domain is discretized using a structured mesh created in OpenFOAM. A uniform mesh with cell size of $0.025H$ is employed from $y/H = -0.5$ to $y/H = 0.833$ to ensure a high mesh resolution in the region of interest near the print zone. Upstream and downstream of this region, geometric growth rates of 1.05 and 1.03, respectively, are implemented in the y direction to reduce the cell count and the computational cost. In the x and z direction, all cells have length equal to $0.025H$. This results in a mesh with over 5 million cells.

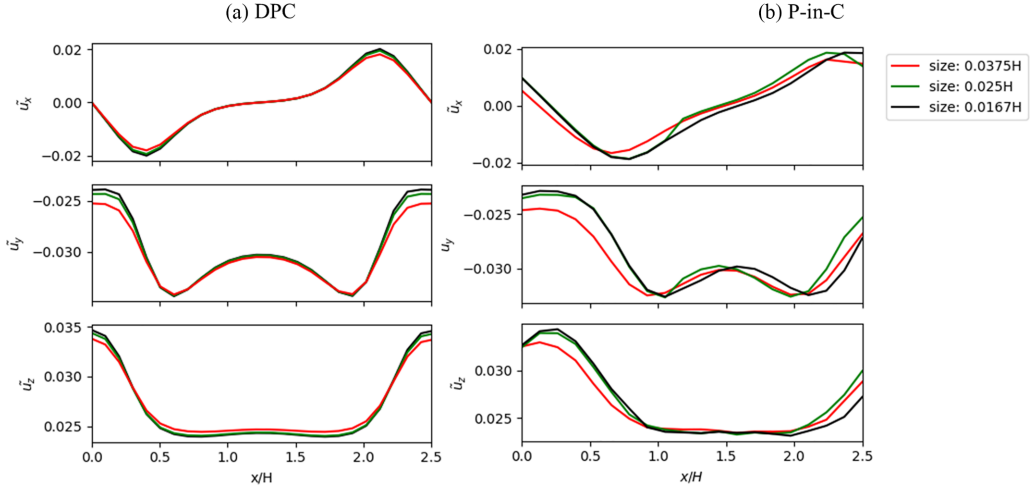


FIG. 5. Comparison of velocity profiles captured by meshes with cell sizes of $0.0167H$, $0.025H$, and $0.0375H$ in simulations using the DPC (a) and P-in-C (b) models.

To assess the error associated with the spatial discretization, tests with meshes with minimum cell size of $0.0167H$, $0.025H$, and $0.0375H$ for a case with $N = 0.355 \times 10^{-3}$, $b/H = 1/3$, $\chi = 0$, $R = 2978$, and $\text{Re}_d = 16$ were compared. The velocity profile captured by a transect extending in the spanwise direction of the domain and located at $y/H = 0$ and $z/H = -0.5$ was used to undertake this comparison. For the DPC model, Fig. 5(a) indicates that these three mesh sizes capture the profile of a standing wave but the coarsest mesh does not capture the same magnitude. Due to the agreement between the two refined meshes, a cell size of $0.025H$ was used to reduce the computational cost of simulations in the present work. For the P-in-C model, however, the mean rms of \tilde{u}_x and the velocity profile are compared to deem convergence. The results indicate that the \tilde{u}_x -rms when using the grid size equal $0.025H$ only differs by 0.5% in comparison to the most refined grid, while the coarsest mesh presents a difference of 12%. Figure 5(b) also indicates that the grids with cell size of $0.025H$ and $0.0375H$ correlate well. It is believed, thus, any improvements provided by a more refined mesh do not seem to compensate the increase of over $2\times$ in computational time and a cell size of $0.025H$ was used to perform the analyses presented here.

G. Temporal discretization

Time steps of $\Delta\tilde{t} = 0.25$, 0.1 , and 0.05 , where \tilde{t} is the droplet transit time defined by H/W , in a case with $N = 0.355 \times 10^{-3}$, $b/H = 1/3$, $\chi = 0$, $R = 2978$, and $\text{Re}_d = 16$ were tested. For the DPC model, since the airflow converges to a steady-state solution, a steady version of the model was also compared against the transient analyses. The velocity profile captured by the transect located at $y/H = 0$ and $z/H = -0.5$ [Fig. 6(a)] indicates that the steady solver efficiently captures the flow profile without introducing any errors due to the lack of temporal resolution.

For the P-in-C model, however, due to its nature, the simulations must be transient. To assess the error associated with the temporal discretization, the time average of the rms of \tilde{u}_x was computed for time steps of $\Delta\tilde{t} = 0.1$, 0.25 , and 0.5 . It was observed that the mean rms of \tilde{u}_x captured when using a time step of $\Delta\tilde{t} = 0.25$ only differed by less than 1% in comparison to the simulations with $\Delta\tilde{t} = 0.1$, whereas the rms of \tilde{u}_x for $\Delta\tilde{t} = 0.5$ differs by 1.9%. Figure 6(b) also shows that the results with $\Delta\tilde{t} = 0.25$ correlate well to the simulation with $\Delta\tilde{t} = 0.1$ and, as a result, the following P-in-C numerical analyses are performed with $\Delta\tilde{t} = 0.25$.

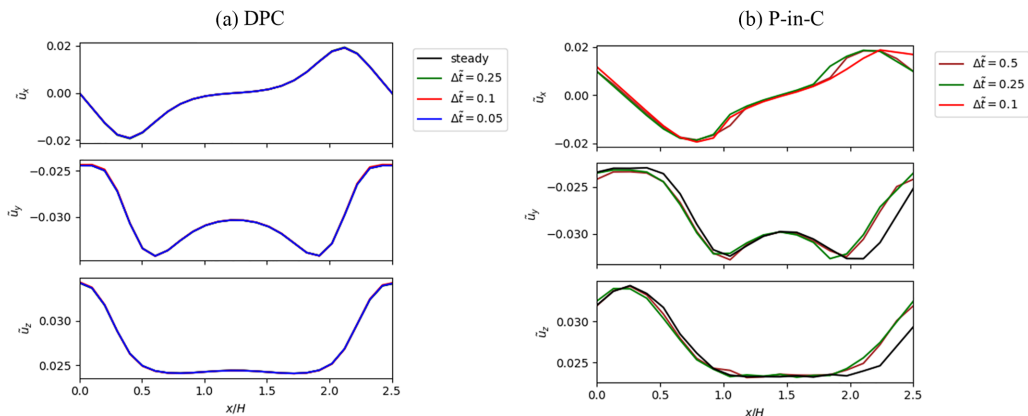


FIG. 6. Comparison of velocity profiles in steady-state and transient simulations with time step of $\Delta\tilde{t} = 0.25, 0.1, \text{ and } 0.05$.

III. RESULTS

A. Investigating the DPC assumptions

A case with $N = 0.267 \times 10^{-3}$, $V_p/W = 0.027$, $b/H = 1/3$, and $\chi = 0$ was initially used to assess the assumptions implemented in the DPC model. In previous studies [4,12,14], the DPC model approximated the droplet velocity to constant and equal to the ejection velocity. The results computed using the DPC model were compared against snapshots and the time average of the flow field computed by the P-in-C model. The time average of the statistically stationary interval creates a more homogeneous flow field and facilitates the comparison between the DPC and P-in-C models.

The \bar{Q} criterion at a vertical plane located at $x/H = 0.9375$ for a case with $N = 0.267 \times 10^{-3}$, $V_p/W = 0.027$, and $b/H = 1/3$ demonstrates that both models capture two counter-rotating vortices (**A** and **B**) with the upstream vortex (**A**) being more concentrated (Fig. 7). The P-in-C snapshot at $\tilde{t} = 5 \times 10^4$ [Fig. 7(c)] tends to show a distorted and quite *spotty* \bar{Q} -criterion flow field (**C**) as a result of the instantaneous relative motion between particles, while the time-averaged data shows a more homogeneous field but with some residual spottiness [Fig. 7(d)]. The DPC model, however, tends to overpredict the strength and size of the counter-rotating vortices [Fig. 7(a)]. This is a result of the constant dispersed phase velocity field assumption initially used in the DPC model. This is further confirmed in Fig. 8 that shows the droplets decelerating to 0.51 of their initial velocity, resulting in significant loss in momentum.

To account for the droplet deceleration in the DPC model, a one-way formulation first estimates the final velocity of a single particle when moving in still air for a distance H . This was achieved by integrating the equations of motion [Eqs. (6) and (7)] over time until the particle had traveled the specified distance. It was assumed that the only force acting on the particle is the drag which is modeled with the Stokes law multiplied by White's empirical correction factor. This formulation gave an error of approximately 1% in comparison to the final velocity computed by the P-in-C model. Once this process was performed, the droplet deceleration was implemented in the DPC model by assuming that \mathbf{u}_d in Eq. (8) varies linearly from the ejection velocity to the final velocity. The use of a linear interpolation is deemed as acceptable since the droplet velocity variation during flight differs only marginally from a straight line, which is confirmed by the studies of [11].

When the DPC model accounts for the droplet deceleration, the flow structures better correlate to those seen in the P-in-C model. The strength and size of the vortices are equivalent in both models [Fig. 7(b)]. A transect taken in the longitudinal direction of the domain at $x/H = 0.9375$ and $z/H = -0.5$ quantitatively characterizes the correlation between the models. Figure 9 clearly

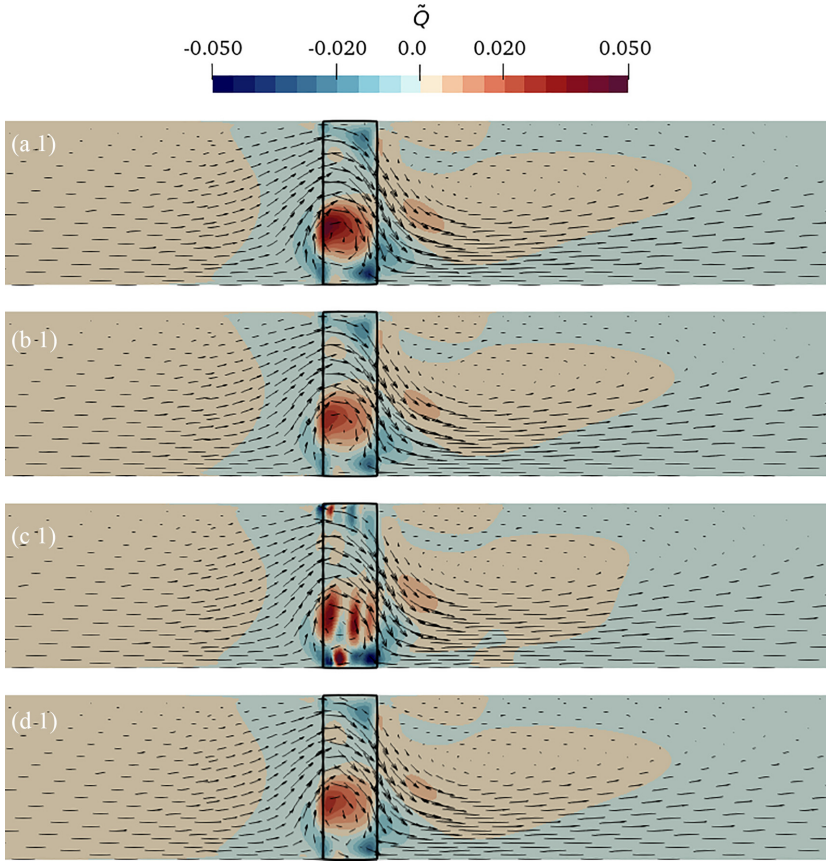


FIG. 7. Vector field overlaid on \tilde{Q} -criterion contour comparing the DPC and P-in-C models at a vertical plane located at $x/H = 0.9375$ for a case with $N = 0.267 \times 10^{-3}$, $V_p/W = 0.027$, $b/H = 1/3$, and $\chi = 0$; (a) DPC model that disregards the droplet deceleration, (b) DPC that accounts for droplet deceleration, (c) P-in-C snapshot at $\tilde{t} = 5 \times 10^4$, and (d) P-in-C time averaged. **A**, **B**, and **C** are, respectively, the upstream and downstream vortices and the vortex spottiness. Paper moving from left to right.

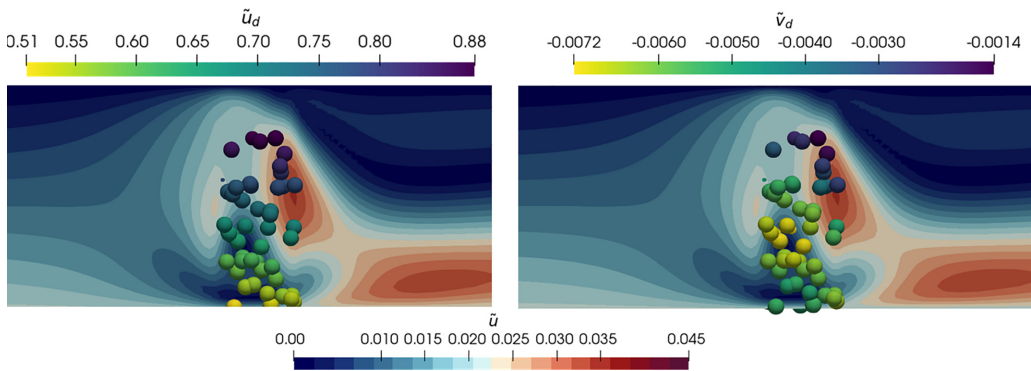


FIG. 8. Point particles colored by their velocity magnitude (left) and horizontal velocity (right) overlaid on the flow field velocity magnitude contour indicating the droplets' velocity variation as they transit across the print gap. Paper moving from left to right.

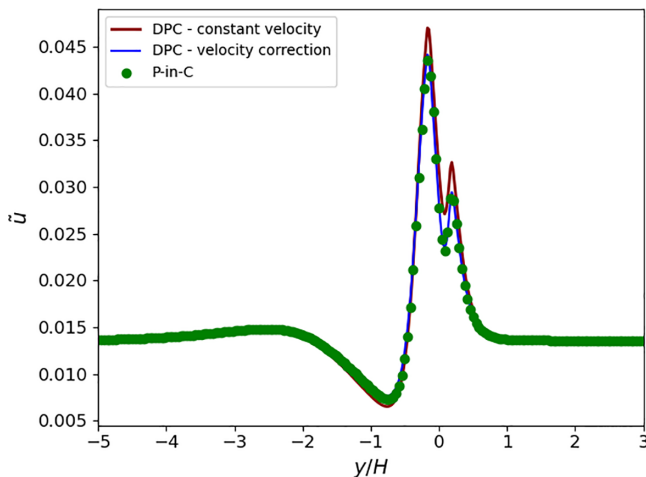


FIG. 9. Velocity magnitude measured by a longitudinal transect located $x/H = 0.9375$ and $z/H = -0.5$ comparing the DPC with and without droplet velocity correction (dark red and blue lines, respectively) and P-in-C (green dots) for a case with $N = 0.267 \times 10^{-3}$, $V_p/W = 0.027$, $b/H = 1/3$, $\chi = 0$, $R = 2978$, and $Re_d = 16$.

indicates that the DPC with droplet deceleration shows a strong correlation to the P-in-C model. The DPC captures well both the maximum velocity and the gradient of velocity. Further investigations of the main droplet velocity indicate that, for the paper speed and through flow tested here, the droplets longitudinal velocity reaches up to 0.14% of the ejection velocity. Given the transit time of the droplets, it is estimated that their longitudinal displacement does not exceed $6.67 \times 10^{-4}H$. This demonstrates that the incoming cross flow minimally displaces the droplets during flight and, as a result, it is expected that there is no substantial need to account for the longitudinal displacement of droplets nor their longitudinal velocity in the DPC model.

The agreement between the DPC and P-in-C model is a strong indicator that treating the discrete phase as a continuum smooth field is a valid strategy to compute the mean flow field. The main difference between the two models comes from the *spottiness* predicted using the P-in-C model that is a result of the local and instantaneous slip velocity of the particles that perturbs the base flow (Fig. 10). The FFT of the stationary interval of the velocity signal measured by a probe located at $x/H = 0.9375$, $y/H = 0$, and $z/H = -0.5$ is used to characterize the airflow spottiness. It is seen that the spottiness manifests as a dense spectrum with no peak in Strouhal number ($St = f_n H/W$) and where the power density decays with St . The spottiness, although existent in real printing systems, is not expected to directly induce the tiger stripes printing defects. This is because this printing defect is characterized by specific time and length scales while the spottiness behaves as noise. The specificity of the time and length scales are the factors that contribute to the objectionability of the printing defects as the human eye is very perceptive of patterns while tolerant to blur or noise [27].

B. Bifurcation diagram

The effectiveness of the DPC model for predicting the range of the flow regimes is investigated by characterizing the airflow response to an array of cases defined by different number densities (N). We note that this study extends the work done in two dimensions [4,14] to a three-dimensional (3D) domain, while also assessing the accuracy of the DPC model. Cases with $V_p/W = 0.027$, $b/H = 1/3$, and number density ranging from $N = 0.267 \times 10^{-3}$ to $N = 0.355 \times 10^{-3}$ are performed in an attempt to reproduce some of the conditions that the market currently demands.

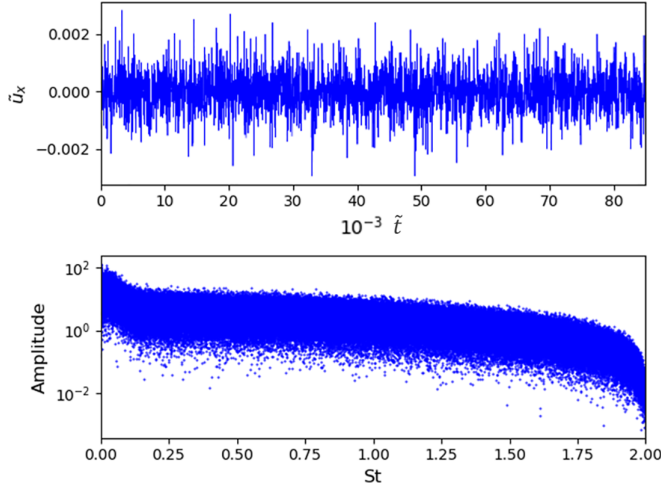


FIG. 10. Top: x -velocity signal measured by a probe located at $x/H = 0.9375$, $y/H = 0$, and $z/H = -0.5$; bottom: DFT of the velocity signal showing the frequency behavior of the spottiness. Printing conditions: $N = 0.267 \times 10^{-3}$, $V_p/W = 0.027$, $b/H = 1/3$, $\chi = 0$, $R = 2978$, and $Re_d = 16$.

For low number densities, the flow field captured by the DPC model is uniform in time and spanwise direction. The base flow field is characterized by a pair of spanwise-uniform counter-rotating vortices as indicated in Figs. 7 and 11(b1) and described by Aquino *et al.* [4]. Due to the interaction with the incoming cross flow, the upstream vortex, referred to as the main vortex, is more concentrated than the downstream vortex. The main vortex extends across the spanwise direction of the domain forming a nearly cylindrical shape.

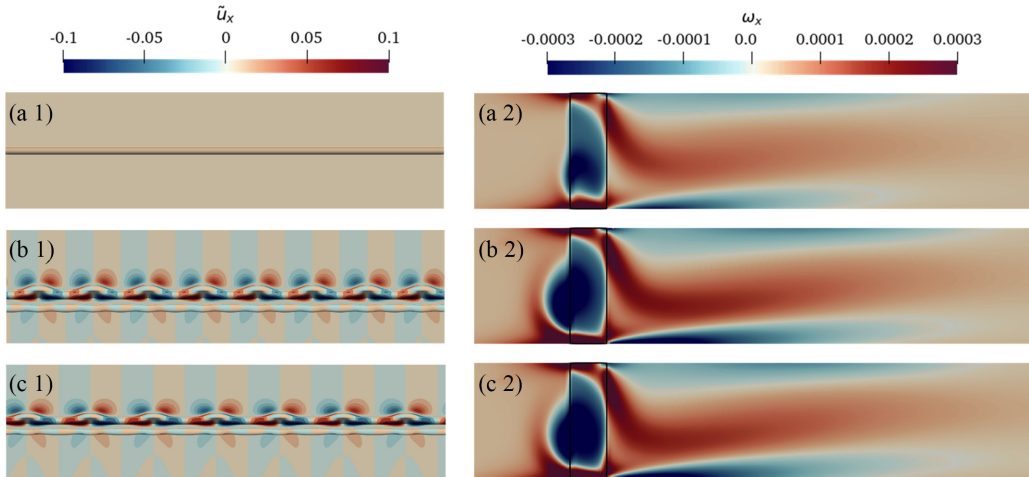


FIG. 11. On the left side: top view of an xy plane located at $z/H = -0.5$ showing isosurface of \bar{Q} criterion overlaid on a plane located at $z/H = -0.5$ and colored by \tilde{u}_x comparing, while on the right side: $\tilde{\omega}_x$ contour at a vertical plane located at $x/H = 0.9375$; both set of plots comparing (a) spanwise-uniform flow field regime with $N = 0.267 \times 10^{-3}$, (b) standing wave regime for a case with $N = 0.267 \times 10^{-3}$ and $\lambda/H = 1.667$, and (c) standing wave regime for a case with $N = 0.267 \times 10^{-3}$ and $\lambda/H = 2.667$. Printing conditions: $V_p/W = 0.027$, $b/H = 1/3$, $\chi = 0$, $R = 2978$, and $Re_d = 16$. Paper moving from top to bottom.

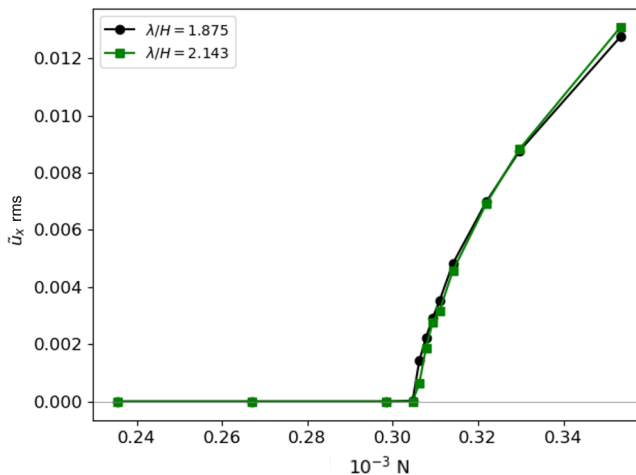


FIG. 12. Bifurcation diagram showing the transition from uniform flow to standing wave regime for DPC solutions with wavelength $\lambda/H = 2.143$ and 1.875 at $b/H = 1/3$, $V_p/W = 0.027$, $\chi = 0$, $R = 2978$, and $\text{Re}_d = 16$.

For high number densities, the vortices become stronger due to the higher entrainment effect and their cores become deformed, and a standing wave pattern is evident (Fig. 11). This standing wave is characterized by a specific wave number. Two possible different solutions with seven and eight wave number have been captured by the model with the imposed span of $15H$, which translates to wavelengths (λ) of $\lambda/H = 2.143$ and 1.875 , respectively. The wavelength measured in the simulations correlates well to that of the prints performed at Memjet, which range from $\lambda/H = 1.667$ to 2.667 .

To characterize the range of flow regimes (spanwise-uniform flow field and standing wave), the root mean square (rms) of \tilde{u}_x measured by a spanwise transect located at $y/H = 0$ and $z/H = -0.5$ is employed. It is seen in Fig. 12 that, for each solution ($\lambda/H = 2.143$ and 1.875), there is a bifurcation point or critical print density (N_c) at which the rms shifts from zero to a finite value, indicating that the airflow transitions from the uniform regime to the standing wave regime. At the critical print density, the disturbance induced by the entrainment effect promotes an exchange of stability that characterizes a supercritical pitchfork bifurcation [28]. The two solutions have similar bifurcation diagrams that define the exchange of stability. While the solution with $\lambda/H = 2.143$ transitions at $N_c = 0.306 \times 10^{-3}$, the solution with $\lambda/H = 1.875$ bifurcates at $N_c = 0.305 \times 10^{-3}$. It is also observed that, for $\lambda/H = 2.143$, the rms of the standing wave reaches higher magnitudes. These results show that the transition to the standing wave regime in a 3D domain occurs at lower number densities than the supercritical Hopf bifurcation captured in a 2D domain, which occurred at $N_c = 1.30 \times 10^{-3}$. We note here that, to compute the two possible solutions, the cases were initialized with either a Couette–Poiseuille flow field or through numerical continuation [29].

For the comparison between the DPC and the P-in-C, a domain with $w = 1.875H$ width is used. This is because of the larger computational cost of the P-in-C and the long realization time to reach statistical stationarity. The comparison between the DPC and the P-in-C models for a case with $N = 0.355 \times 10^{-3}$ shows excellent agreement. Figure 13 shows that the time-averaged P-in-C captures the same flow field pattern and the same vortex deformation as that observed in the DPC. The P-in-C snapshot at $\tilde{t} = 10^5$ [Fig. 13(c)] shows that the spottiness tends to create a corrugated deformed vortex without significantly altering the downstream \tilde{u}_x flow field magnitude. A longitudinal transect at $y/H = 0$ and $z/H = -0.5$ (Fig. 14) confirms the agreement between the time-averaged P-in-C and DPC. It is observed that the time-averaged P-in-C shows a similar standing wave profile as that of the DPC but the profile tends to have a 3% lower amplitude.

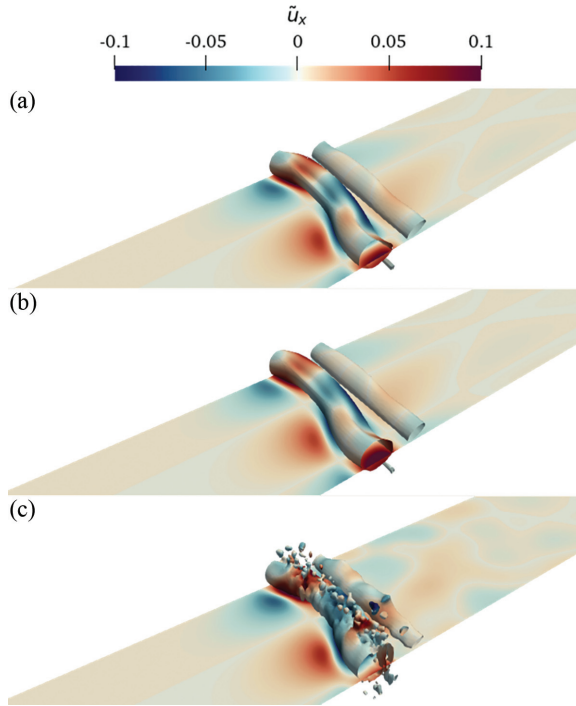


FIG. 13. Isosurface of \tilde{Q} criterion overlaid on a plane located at $z/H = -0.5$ and colored by \tilde{u}_x , comparing the DPC ($\lambda/H = 1.875$) and P-in-C for a case with $b/H = 1/3$, $V_p/W = 0.027$, $N = 0.355 \times 10^{-3}$, $\chi = 0$, $R = 2978$, and $\text{Re}_d = 16$. (a) DPC solution, (b) P-in-C time average, and (c) snapshot at $\tilde{t} = 10^5$. Paper moving from left to right.

The bifurcation diagram when using the P-in-C differs from the DPC diagram as it shows a smooth continuous curve rather than a transition point. (See Fig. 15.) The DPC and P-in-C agree well for number densities above the transition point. However, at low number densities, below and near the transition point, the P-in-C shows a nonzero rms, which is a result of the spottiness that perturbs the flow field. This is because the standing wave mode is repeatedly excited by the stochastic forcing spottiness and the balance between the forcing and the rate of decay leads to a nonzero mean at statistical stationarity. Systems subjected to a stochastic excitation have already been observed to have a similar response [30,31]. For instance, in the study of a horizontal pendulum [28], it was demonstrated that the system presented a supercritical pitchfork bifurcation when the pendulum was pushed by a sinusoidal force but, when the force was perturbed by a stochastic noise, the bifurcation diagram became a smooth continuous curve in what has been referred to as a perturbed supercritical pitchfork bifurcation. To investigate the discrepancies between the DPC and the P-in-C at low number densities, the isosurface of \tilde{Q} criterion overlaid on a plane located at $z/H = -0.5$ and colored by \tilde{u}_x for a case with $N = 0.267 \times 10^{-3}$ is exhibited in Fig. 16. The isosurface computed by the P-in-C shows that the standing wave vortex core deformation is minimal and nearly unnoticeable in comparison to the lumps created by the spottiness. The contour of \tilde{u}_x shows that the magnitude of \tilde{u}_x tends to be close to zero. However, the flow field starts to demonstrate the patterns observed in the case with $N = 0.355 \times 10^{-3}$ (Fig. 13), where the lateral velocity shows a sinusoidal variation from positive to negative.

The DPC model serves, thus, as a means of predicting the time averaged flow features and approximating the evolution of the standing wave regime while also being much more computationally efficient than the P-in-C model. The DPC model takes no more than 1.5 h when run on 96

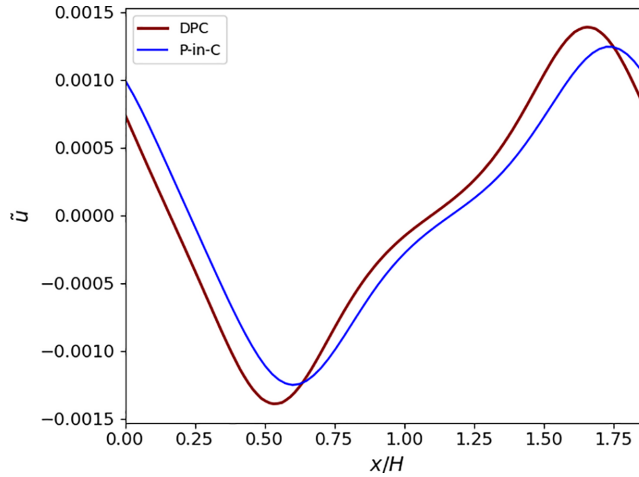


FIG. 14. Lateral velocity profile taken at a spanwise transect located at $y/H = 0$ and $z/H = -0.5$ for a case with $b/H = 1/3$, $V_p/W = 0.027$, $N = 0.355 \times 10^{-3}$, $\chi = 0$, $R = 2978$, and $Re_d = 16$ comparing the DPC ($\lambda/H = 1.875$) and P-in-C models.

processors to reach a steady converged solution for a $15H$ wide domain and approximately 0.2 h for a domain with width of $w = 1.875H$. On the other hand, the P-in-C takes over 240 h to run $\tilde{t} = 10^4$ (40 000 time steps) of simulation when run on the same 96 processors for a full width domain. This simulation time is, however, insufficient to reach statistically meaningful results and increasing the simulation time is unfeasible for the computational resources available. The P-in-C simulations with a domain width of $w = 1.875H$ take approximately 280 h to reach $\tilde{t} = 10^5$ (400 000 time steps) of flow realization. In some cases, the startup effect can take up to $\tilde{t} = 5 \times 10^4$ of realization time, which significantly contributes to the inefficiency of the P-in-C model. The efficiency of the DPC model is due to its formulation that does not track the Lagrangian particle and allows running a steady solver to compute the mean flow field. Such a reduction in computational cost allows a refined search to identify the critical transition point.

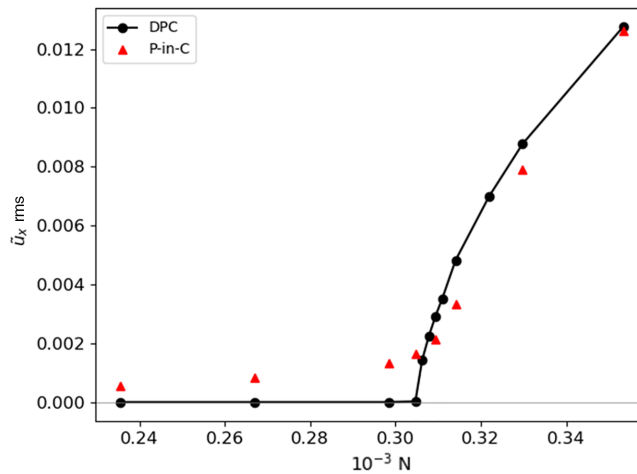


FIG. 15. Bifurcation diagram at $b/H = 1/3$, $V_p/W = 0.027$, $\chi = 0$, $R = 2978$, and $Re_d = 16$ comparing the DPC ($\lambda/H = 1.875$) and P-in-C models.

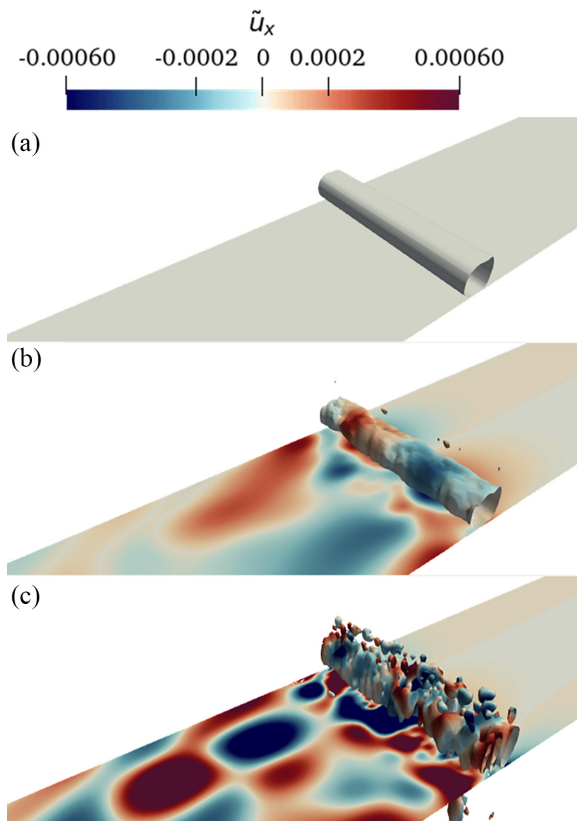


FIG. 16. Isosurface of \tilde{Q} criterion overlaid on a plane located at $z/H = -0.5$ and colored by \tilde{u}_x for a case with $b/H = 1/3$, $V_p/W = 0.027$, $N = 0.267 \times 10^{-3}$, $\chi = 0$, $R = 2978$, and $Re_d = 16$ comparing (a) the DPC with $\lambda/H = 1.875$, (b) P-in-C time averaged, and (c) P-in-C snapshot at $\tilde{t} = 5 \times 10^4$. Paper moving from right to left.

IV. CONCLUSION

Three-dimensional numerical simulations were performed to investigate the effectiveness of the dispersed-phase continuum approximation to model the entrainment effect of the droplets in the print gap of inkjet printers. The results computed by the DPC model were compared against the classic transient particle-in-cell (P-in-C) model. The DPC assumes that, due to the separation in time scales, the dispersed phase can be modeled with a momentum source that depends on a predefined temporally averaged number density field.

Initial tests were performed to assess the assumptions made within the DPC model. It was observed that the droplet deceleration must be accounted for to improve the accuracy of the DPC model. The horizontal motion of the particles, on the other hand, tends to minimally affect the flow field and, as a result, it can be disregarded for the conditions tested in this study. The main difference between the models is that the P-in-C captures the *pseudoturbulence* or *spottiness* created by the instantaneous slip velocity of the particles. The DPC computes a steady flow field that correlates well to the time-averaged solution of the P-in-C model. The main advantage of the DPC model is its efficiency as the computational time to predict the mean flow field is about one fourteen-hundredth of that required for the P-in-C calculation. This is due to the DPC formulation that does not track the particles and the base flow being steady, allowing one to run the DPC model with a steady solver.

Further analyses were performed to characterize the transition from a uniform in time and spanwise direction flow field to a standing wave regime since this sheds light into the printing conditions at which prints are expected to be uniform. While the DPC model captured a critical number density where the flow field shifted from uniform to nonuniform in spanwise direction, the P-in-C model predicted a smooth continuous transition. At number densities above the critical print density, very good correlation was observed between models, but below the critical number density, a certain level of disagreement was exhibited as the P-in-C captured a small and finite standing wave amplitude. This was a result of the *spottiness* that excited the standing wave solution even at low number densities. Thus the DPC model is effective at estimating the time averaged flow features and approximating the evolution of the standing wave regime, while also being dramatically more computationally efficient than the P-in-C model. The reduction in computational cost allows the characterization of the flow field at a wide range of different printing conditions.

ACKNOWLEDGMENTS

We would like to acknowledge Memjet for partially funding this research and the assistance of Dr. D. Stephens, Applied CCM, for assisting with OpenFOAM programing. The numerical analyses were performed in the National Computational Infrastructure (NCI) HPC facilities, which is supported by the Australian Government.

-
- [1] I. Arango, L. Bonil, D. Posada, and J. Arcila, Prediction of a flying droplet landing over a non-flat substrates for ink-jet applications, *Int. J. Interact. Design Manufact.* **13**, 967 (2019).
 - [2] *Fundamentals of Inkjet Printing*, edited by S. D. Hoath (John Wiley & Sons, New York, 2016).
 - [3] *Handbook of Industrial Inkjet Printing*, edited by W. Zapka (Wiley-VCH, New York, 2018).
 - [4] A. F. V. de A. Aquino, S. G. Mallinson, G. D. McBain, G. D. Horrocks, C. M. de Silva, and T. J. Barber, Two-dimensional numerical simulation of inkjet print-zone flows, in *Proceedings of the 22nd Australasian Fluid Mechanics Conference* (The University of Queensland, Brisbane, Australia, 2020).
 - [5] W. K. Hsiao, S. D. Hoath, G. Martin, and I. M. Hutchings, Aerodynamic effects in ink-jet printing on a moving web, in *Proc. NIP28: 28th Int'l. Conf. on Digital Printing Technologies and Digital Fabrication 2012* (Curran Associates, Inc., Red Hook, NY, 2012), pp. 412–415.
 - [6] W.-K. Hsiao, G. D. Martin, S. D. Hoath, I. M. Hutchings, M. Hook, and M. Massucci, Evidence of print gap airflow affecting web printing quality, in *Proc. NIP29: 29th Int'l. Conf. on Digital Printing Technologies and Digital Fabrication 2013* (Curran Associates, Inc., Red Hook, NY, 2013), pp. 303–306.
 - [7] S. G. Mallinson, G. D. McBain, G. D. Horrocks, A. J. North, A. P. O'Mahony, P. J. Reichl, S. J. Myers, J. J. Miller, B. Powell, J. Hess, D. R. Secker, and P. C. Palma, Suppressing tiger stripes: Taming flow oscillations to improve print quality, in *Proceedings of the 20th Australasian Fluid Mechanics Conference* (The University of Queensland, Brisbane, Australia, 2016).
 - [8] S. G. Mallinson, A. F. V. de A. Aquino, G. D. McBain, G. D. Horrocks, T. J. Barber, C. M. de Silva, and G. Yeoh, Three-dimensional numerical simulation of air-flow in inkjet print-zones, in *Proceedings of the 22nd Australasian Fluid Mechanics Conference* (The University of Queensland, Brisbane, Australia, 2020), pp. 2–5.
 - [9] C. Rodriguez-Rivero, J. R. Castrejón-Pita, and I. M. Hutchings, Aerodynamic effects in industrial inkjet printing, *J. Imaging Sci. Technol.* **59**, 040401-1 (2015).
 - [10] S. Wang, Aerodynamic effect on inkjet main drop and satellite dot placement, in *Proc. NIP14: 14th Int'l. Conf. on Digital Printing Technologies and Digital Fabrication* (Curran Associates, Inc., Red Hook, NY, 1999), pp. 5–9.
 - [11] D. Barnett and M. McDonald, Evaluation and reduction of elevated height printing defects, in *Proc. NIP30: 30th Int'l. Conf. on Digital Printing Technologies and Digital Fabrication 2014* (Curran Associates, Inc., Red Hook, NY, 2014), pp. 38–43.

- [12] S. G. Mallinson, A. F. V. de A. Aquino, G. D. McBain, G. D. Horrocks, T. J. Barber, C. M. de Silva, and G. H. Yeoh, Three-dimensional numerical simulation of air-flow in inkjet print-zones, *Int. J. Heat Fluid Flow* **93**, 108911 (2022).
- [13] Memjet is a multinational inkjet printer manufacturer and research partner in this project, <https://www.memjet.com/>.
- [14] A. F. V. de A. Aquino, S. G. Mallinson, G. D. McBain, G. D. Horrocks, C. M. de Silva, and T. J. Barber, Investigation of the vortex instability in a two-dimensional inkjet print-zone using numerical analysis, *Phys. Rev. Fluids* **7**, 013904 (2022).
- [15] H. Iimura and M. Kusunoki, Ink mist behavior analysis in inkjet printer, *J. Imaging Soc. Jpn.* **56**, 473 (2017).
- [16] J. M. Kuerten, Point-particle dns and les of particle-laden turbulent flow—a state-of-the-art review, *Flow, Turbul. Combust.* **97**, 689 (2016).
- [17] H. Nasr, G. Ahmadi, and J. B. McLaughlin, A dns study of effects of particle–particle collisions and two-way coupling on particle deposition and phasic fluctuations, *J. Fluid Mech.* **640**, 507 (2009).
- [18] M. C. Baker, B. Kong, J. Capecehatro, O. Desjardins, and R. O. Fox, Direct comparison of Eulerian–Eulerian and Eulerian–Lagrangian simulations for particle-laden vertical channel flow, *AIChE J.* **66**, e16230 (2020).
- [19] A. Vié, H. Pouransari, R. Zamansky, and A. Mani, Particle-laden flows forced by the disperse phase: Comparison between Lagrangian and Eulerian simulations, *Int. J. Multiphase Flow* **79**, 144 (2016).
- [20] R. Keser, V. Vukčević, M. Battistoni, H. Im, and H. Jasak, Implicitly coupled phase fraction equations for the Eulerian multi-fluid model, *Comput. Fluids* **192**, 104277 (2019).
- [21] R. Seydel, *Computational Methods for Multiphase Flow* (Cambridge University Press, Cambridge, UK, 2007).
- [22] F. M. White and I. Corfield, *Viscous Fluid Flow* (McGraw-Hill, New York, 1991).
- [23] T. Holzmann, *Mathematics, Numerics, Derivations and OpenFOAM* (John Wiley & Sons, New York, 2016).
- [24] R. Fletcher, Conjugate gradient methods for indefinite systems, in *Numerical Analysis*, Notes in Mathematics (Springer, Berlin, 1976), pp. 73–89.
- [25] T. Behrens, Openfoam’s basic solvers for linear systems of equations: Solvers, preconditioners, smoothers, www.tfd.chalmers.se/~hani/kurser/OS_CFD_2008/TimBehrens/tibeh-report-fin.pdf.
- [26] J. Brouwer, J. Tukker, M. Van Rijsbergen *et al.*, Uncertainty analysis of finite length measurement signals, in *The 3rd International Conference on Advanced Model Measurement Technology for the EU Maritime Industry (AMT’13)*, Gdansk, Poland (2013), pp. 260–274.
- [27] G. Sharma and R. Bala, *Digital Color Imaging Handbook* (CRC Press, Boca Raton, FL, 2017).
- [28] J. M. Schmitt and P. V. Bayly, Bifurcations in the mean angle of a horizontally shaken pendulum: Analysis and experiment, *Nonlinear Dyn.* **15**, 1 (1998).
- [29] R. Seydel, *Practical Bifurcation and Stability Analysis* (Springer, Berlin, 2009).
- [30] A. Juel, A. G. Darbyshire, and T. Mullin, The effect of noise on pitchfork and hopf bifurcations, *Proc. R. Soc. London A* **453**, 2627 (1997).
- [31] M. F. Schumaker and W. Horsthemke, Imperfect pitchfork bifurcation with weak noise and an application to superfluid turbulence in liquid helium, *Phys. Rev. A* **36**, 354 (1987).